

# How planetary growth outperforms migration

Anders Johansen<sup>1</sup>, Shigeru Ida<sup>2</sup>, & Ramon Brasser<sup>2</sup>

<sup>1</sup> Lund Observatory, Department of Astronomy and Theoretical Physics, Lund University, Box 43, 221 00 Lund, Sweden,  
e-mail: anders@astro.lu.se

<sup>2</sup> Earth-Life Science Institute (ELSI), Tokyo Institute of Technology, Meguro, Tokyo, 152-8550, Japan

## ABSTRACT

Planetary migration is a major challenge for planet formation theories. The speed of Type I migration is proportional to the mass of a protoplanet, while the final decade of growth of a pebble-accreting planetary core takes place at a rate that scales with the mass to the two-thirds power. This results in planetary growth tracks (i.e., the evolution of a protoplanet's mass versus its distance from the star) that become increasingly horizontal (migration-dominated) with rising mass of the protoplanet. It has been shown recently that the migration torque on a protoplanet is reduced proportional to the strength of the gas gap carved by the growing planet. Here we identify that the mass at which a planet carves a 50% gap is approximately 2.3 times the pebble isolation mass, the latter demarking the transition from pebble accretion to gas accretion. Gas accretion to form gas-giant planets therefore takes place over a few astronomical units of migration after reaching first pebble isolation mass and, shortly after, the 50% gap mass. Our results demonstrate how planetary growth can outperform migration, both during core accretion and during gas accretion, even when pebbles are millimeter-sized and the pebble-to-gas flux ratio through the protoplanetary disc is in the nominal range of 0.01–0.02. Reaching a pebble isolation mass of  $\sim 10$  Earth masses by accreting millimeter-sized pebbles is possible provided that pebbles reside in a mid-plane layer with a width of approximately 10% of the gas scale-height, a typical value inferred from observations of protoplanetary discs.

**Key words.** planet-disk interactions, planets and satellites: formation, planets and satellites: gaseous planets

## 1. Introduction

The formation of planets involves many distinct steps in the growth from dust and ice particles to full planetary system (a realisation that was pioneered 50 years ago by Safronov, 1969). The competition between radial migration and growth is nevertheless a general theme in planet formation. The formation of planetesimals, for example, has to overcome the radial drift caused by the head-wind of the slower moving gas on the growing particles (Weidenschilling, 1977; Brauer et al., 2008). Trapping pebbles in pressure bumps formed in the turbulent gas flow (Lyra et al., 2008; Johansen et al., 2009a; Bai, 2015) or by embedded planets (Lyra et al., 2009) or through run-away pile-ups caused by the friction on the gas (Youdin & Goodman, 2005; Johansen et al., 2009b; Bai & Stone, 2010; Gonzalez et al., 2017; Drazkowska et al., 2016) provide possible solutions to the radial drift problem of planetesimal formation.

Planetary migration results from the gravitational torque exerted on a protoplanet by the spiral density wakes excited in the gaseous protoplanetary disc (Lin & Papaloizou, 1979; Goldreich & Tremaine, 1980; Tanaka et al., 2002). The nominal Type I migration rate reaches approximately 1 m/s (about 100 AU/Myr) for a 10-Earth-mass protoplanet embedded in a young, massive protoplanetary disc. The solutions proposed to mitigate catastrophic Type I migration include slowing down or even reversing the migration where the temperature gradient is steep in the inner regions of the protoplanetary disc (Paardekooper et al., 2010; Lyra et al., 2010; Bitsch et al., 2014; Brasser et al., 2017), or by a positive corotation torque resulting from the accretion heat of the protoplanet (Benítez-Llambay et al., 2015) or from the

scattering of (large) pebbles (Benítez-Llambay & Pessah, 2018). Migration can even stall entirely if the turbulent viscosity is too weak to diffuse away the gas density enhancement that forms interior of the planetary orbit (Rafikov, 2002; Li et al., 2009; Fung & Lee, 2018).

A more direct way to overcome Type I migration is simply for the planetary core to increase its mass very rapidly. The accretion rate of pebbles is potentially high enough for the protoplanet growth to outperform the nominal rate of Type I migration (Lambrechts & Johansen, 2014; Ormel et al., 2017; Johansen & Lambrechts, 2017). Bitsch et al. (2015b) demonstrated that protoplanets forming several tens of AU from the host star have enough space to grow to gas-giant planets while they migrate into 5–10 AU orbits<sup>1</sup>. However, Brügger et al. (2018) found that the pebble flux rate in the model of Bitsch et al. (2015b) was artificially high and that nominal pebble fluxes ( $\sim 0.01$  relative to the gas flux) do not yield high enough core growth rates to compete with migration, unless the metallicity is enhanced significantly beyond the solar value. Bitsch et al. (2018a) argued instead that the pebble sizes and surface densities of Bitsch et al. (2015b) in fact correspond well to observations of protoplanetary discs. However, although the protoplanetary disc model advocated in Bitsch et al. (2018a) is motivated observationally, the pebble sizes and surface densities used in that work are not anchored in self-consistent theoretical models of pebble growth and drift.

In this paper we develop pebble accretion models with millimeter-sized pebbles, much smaller than those considered in Bitsch et al. (2015b) and Brügger et al. (2018). Such small pebbles follow the viscous accretion flow of the gas and, in con-

<sup>1</sup> Matsumura et al. (2017), on the other hand, started the seeds in the 5–10 AU region and showed how this leads mainly to the formation of warm and hot Jupiters

trast to larger pebbles, their column density is not reduced by radial drift (Lambrechts & Johansen, 2014). We demonstrate how in this model planetary formation outperforms migration for nominal pebble fluxes and metallicities. We derive analytical expressions that describe the growth tracks of solid protoplanets undergoing pebble accretion (Section 2 and Appendix A). We find that planetary cores do undergo substantial migration before reaching the pebble isolation mass. However, using novel prescriptions for the migration rate of gap-opening planets (Kanagawa et al., 2018), we show that gas accretion to form gas-giant planets takes place over just a few astronomical units of migration (Section 3). Hence the main migration phase of a protoplanet happens during the accumulation of the core. We summarise our results and discuss the implications for planet formation in Section 4. Our paper forms a companion paper to Ida et al. (2018), which focuses on the effect of the Kanagawa et al. (2018) migration rate on the gas accretion stage.

## 2. Analytical pebble accretion growth tracks

In this section we derive analytical expressions for the growth track of a protoplanet growing by pebble accretion. We then use this expression to derive the location where the growth track crosses the pebble isolation mass.

### 2.1. Pebble accretion

To derive the analytical shape of the growth track of a solid protoplanet, we use the protoplanet growth rate from pebble accretion in the 2-D Hill regime (Ormel & Klahr, 2010; Lambrechts & Johansen, 2012; Ida et al., 2016),

$$\dot{M} = 2 \left( \frac{\text{St}}{0.1} \right)^{2/3} \Omega R_H^2 \Sigma_p. \quad (1)$$

Here  $M$  is the mass of the protoplanet,  $\text{St} = \Omega \tau_f$  is the Stokes number of the pebbles (defined later in equation 16),  $\Omega$  is the Keplerian frequency at the location of the protoplanet,  $\tau_f$  is the friction time of the pebble (proportional to the particle size when pebbles are small),  $R_H = [M/(3M_\star)]^{1/3} r$  is the Hill radius of the protoplanet,  $M_\star$  is the mass of the central star,  $r$  is the radial location of the planet and  $\Sigma_p$  is the pebble surface density. Significant effort is currently being put into understanding how pebble accretion depends on the eccentricity and inclination of the protoplanet (Johansen et al., 2015; Liu & Ormel, 2018) as well as on realistic hydrodynamical flow in the Hill sphere (Popovas et al., 2018), but we consider here the relatively simpler case of a protoplanet on a circular orbit and the gas flow as pure shear.

Our assumption of 2-D Hill accretion is valid when the pebble accretion radius,  $R_{\text{acc}} = (\text{St}/0.1)^{1/3} R_H$ , is larger than the scale-height of the pebble layer,  $H_p = H \sqrt{\delta/\text{St}}$  (see Morbidelli et al., 2015, for a discussion). Here  $H$  is the scale-height of the gas and  $\delta$  is the dimensionless dust diffusion coefficient (defined in Johansen et al., 2014). That gives an accretion radius relative to the pebble scale-height as

$$\frac{R_{\text{acc}}}{H_p} = 0.9 \left( \frac{\text{St}}{0.01} \right)^{1/3} \left( \frac{M}{M_E} \right)^{1/3} \left( \frac{H/r}{0.05} \right)^{-1} \left( \frac{\text{St}/\delta}{100} \right)^{1/2}. \quad (2)$$

We normalised here to  $\text{St} = 0.01$  and  $\delta = 0.0001$ . Our choice of Stokes number  $\text{St} = 0.01$  is elaborated in Section 2.4, while the choice of a low diffusion coefficient  $\delta$  is motivated by observations of dusty protoplanetary discs that show that the dust

has settled to a mid-plane layer of width 10% of a gas scale-height (Mulders & Dominik, 2012; Menu et al., 2014; Pinte et al., 2016). Note that  $\text{St}/\delta = 100$  indeed yields a moderately sedimented pebble mid-plane layer with a scale-height relative to the gas scale-height of  $H_p/H = 0.1$ .

The transition from the Bondi regime (where the pebble approach speed is set by the sub-Keplerian motion) to the Hill regime (where the pebble approach speed is set by the Keplerian shear) of pebble accretion typically happens at 0.001-0.01 Earth masses (Lambrechts & Johansen, 2012). Protoplanets that accrete either in the Bondi regime or in the 3-D Hill regime thus experience very low migration rates and hence the shape of the growth track is not affected by our choice to start the analytical core growth tracks in the 2-D Hill accretion phase. In Section 3 we include the 3-D branch of Hill accretion in the numerical integrations.

Johansen & Lambrechts (2017) demonstrated that the accretion of planetesimals contributes significantly to the growth from planetesimal sizes to protoplanets with masses 0.001 – 0.01  $M_E$ , due to the low rates of pebble accretion in the Bondi regime, while pebble accretion in the Hill regime dominates the further growth. Therefore we start our protoplanets at  $M_0 = 0.01 M_E$  and ignore the contribution of planetesimal accretion to the core growth rate, although the inclusion of planetesimal accretion could give a boost to the accretion rate, depending on the migration speed of the protoplanet (Tanaka & Ida, 1999).

### 2.2. Type I migration

For Type I migration we use the standard scaling law,

$$\dot{r} = -k_{\text{mig}} \frac{M}{M_\star} \frac{\Sigma_g r^2}{M_\star} \left( \frac{H}{r} \right)^{-2} v_K. \quad (3)$$

Here  $\dot{r}$  is the migration speed of the protoplanet,  $k_{\text{mig}}$  is a constant prefactor that depends on the gradients of surface density and temperature,  $M_\star$  is the mass of the central star,  $\Sigma_g$  is the gas surface density,  $H/r$  is the disc aspect ratio and  $v_K$  is the Keplerian speed at the position of the planet. For the prefactor  $k_{\text{mig}}$  we follow here a fit to 3-D numerical simulations found in D’Angelo & Lubow (2010),

$$k_{\text{mig}} = 2(1.36 + 0.62\beta + 0.43\zeta), \quad (4)$$

where  $\beta$  and  $\zeta$  are the negative logarithmic derivatives of the surface density and the temperature profiles, respectively. However, we explicitly maintain  $k_{\text{mig}}$  in our equations, since the prefactor depends on the physical effects that are included in the simulations (e.g. Tanaka et al., 2002; Paardekooper et al., 2010).

### 2.3. Radial mass fluxes of gas and pebbles

The gas sound speed  $c_s$  and the derived gas scale-height  $H = c_s/\Omega$  enter both the calculation of the planetary migration rate as well as expressions for the radial speed of the gas and pebbles that we present below. We assume that the sound speed profile follows a power law

$$c_s = c_{s1} \left( \frac{r}{\text{AU}} \right)^{-\zeta/2}. \quad (5)$$

Here  $\zeta$  is the negative power-law index of the temperature (proportional to  $c_s^2$ ) and  $c_{s1}$  is the sound speed at 1 AU. The disc aspect ratio then follows the power-law

$$\frac{H}{r} \propto r^{-\zeta/2+1/2}. \quad (6)$$

The turbulent viscosity  $\nu$  sets the radial gas accretion speed. We use here the  $\alpha$ -disc assumption for the turbulent viscosity (e.g. Pringle, 1981),

$$\nu = \alpha c_s H. \quad (7)$$

This now results in the gas accretion speed

$$u_r = -\frac{3}{2} \frac{\nu}{r} = -\frac{3}{2} \alpha c_s \frac{H}{r}. \quad (8)$$

This expression for the accretion speed is specific to the  $\alpha$ -disc assumption and would not be valid if the angular momentum loss was carried instead by disc winds (Bai & Stone, 2013). However, since the radial mass accretion rate of the gas depends only on the speed of the gas, and not on the nature of the angular momentum transport, we can consider  $\alpha$  in equation (8) simply a dimensionless measure of the radial accretion speed.

The radial drift of the particles is given by (Weidenschilling, 1977)

$$v_r = -\frac{2\Delta v}{St + St^{-1}} + \frac{u_r}{1 + St^2}. \quad (9)$$

In the limit  $St \ll 1$ , valid for pebbles smaller than approximately 0.1-1 meters in size outside of a few AU (Johansen et al., 2014), this expression simplifies to

$$v_r = -2St\Delta v + u_r. \quad (10)$$

Here the sub-Keplerian speed  $\Delta v$ , which is a measure of the radial pressure support of the gas, is given by

$$\Delta v = -\frac{1}{2} \frac{H}{r} (\partial \ln P / \partial \ln r) c_s. \quad (11)$$

We denote the negative logarithmic pressure gradient in the mid-plane as  $-\partial \ln P / \partial \ln r \equiv \chi = \beta + \zeta/2 + 3/2$ . The inwards mass fluxes of gas and pebbles, respectively, are given by

$$\dot{M}_g = -2\pi r u_r \Sigma_g, \quad (12)$$

$$\dot{M}_p = -2\pi r v_r \Sigma_p. \quad (13)$$

The ratio of the surface densities of pebbles to gas is then

$$\frac{\Sigma_p}{\Sigma_g} = \frac{\dot{M}_p}{\dot{M}_g} \frac{u_r}{-2St\Delta v + u_r} = \frac{\xi}{(2/3)(St/\alpha)\chi + 1}. \quad (14)$$

Here we defined the ratio of the fluxes as in Ida et al. (2016),

$$\xi = \frac{\dot{M}_p}{\dot{M}_g}. \quad (15)$$

We will show below in Sections 2.5 and 2.6 that  $\xi$  is a key parameter that determines the shape of a protoplanet's growth track and the total migration distance of the protoplanet before reaching the pebble isolation mass. The gas and solid components of the protoplanetary disc will accrete towards the star at the same time-scale when  $\xi \approx 0.01$ , where 0.01 represents the metallicity  $Z$  of the protoplanetary disc. This nominal value of  $\xi$  is obtained when the radial drift of the pebbles is dominated by advection with the accreting gas, corresponding to  $St/\alpha \lesssim 1$  in equation (14). Therefore also the local metallicity  $\Sigma_p/\Sigma_g$  will keep its original value  $Z$  for the nominal pebbles-to-gas flux ratio.

Large pebbles with  $St \gg \alpha$  in equation (14) experience an increase in  $\xi$  proportional to  $St$  and hence the local metallicity  $\Sigma_p/\Sigma_g$  is maintained at its global value  $Z$ . An increased Stokes number will nevertheless have an overall positive effect on the

pebble accretion rate (through equation 1), but such large pebbles are lost to radial drift on a shorter time-scale than the gas accretion. This is the well-known radial drift problem of protoplanetary discs (Brauer et al., 2007). Another possibility is that  $\xi$  is dictated by the production rate of pebbles in the outer regions of the protoplanetary disc (Lambrechts & Johansen, 2014; Bitsch et al., 2015b). In that case  $\xi$  is no longer directly coupled to  $St$  in equation (14) and the local metallicity  $\Sigma_p/\Sigma_g$  falls proportional to the inverse Stokes number when  $St \gg \alpha$ . Overall, there are then many advantages to considering small pebbles for pebble accretion models, in contrast to the large pebbles that were used in the models of Bitsch et al. (2015b) and Brügger et al. (2018).

## 2.4. Pebble sizes

Dust in protoplanetary discs grows to pebbles through coagulation (Brauer et al., 2007; Zsom et al., 2010). If particles stick perfectly when they collide, then growth continues until the radial drift time-scale becomes comparable to the growth time-scale, at Stokes numbers around 0.1–1 in the region of giant planet formation (Birnstiel et al., 2012; Lambrechts & Johansen, 2014). Pebble accretion with such drift-limited pebble growth was explored in Bitsch et al. (2015a) and Brügger et al. (2018).

Here we focus instead on a different, and perhaps more realistic, mode of pebble growth where the pebbles experience bouncing or fragmenting collisions. Zsom et al. (2010) showed that the growth of silicate particles is limited to millimeter sizes by bouncing, based on extensive experimental data on collisions between silicate dust aggregates. Such experiments also show that collisions become fragmenting when the collision speed crosses a threshold value (Birnstiel et al., 2012).

Water ice, in contrast to silicates, has higher surface energy and is thus expected to experience growth beyond the bouncing barrier (Okuzumi et al., 2012), while CO<sub>2</sub> ice (and likely CO ice as well) appears to have sticking properties similar to silicates (Musiolik et al., 2016a,b). The CO<sub>2</sub> ice line sits at a temperature of approximately 70 K at solar abundances, corresponding to the 2–4 AU region in the late stages of protoplanetary disc evolution (Bitsch et al., 2015a; Madhusudhan et al., 2017). Hence, we expect that the growth of pebbles is limited by bouncing or fragmentation in the accretion region of the cores of cold gas giants. Ices of CO and CO<sub>2</sub> may, in turn, under UV irradiation form longer refractory organic molecules (Muñoz Caro & Schutte, 2003). We ignore here the possibility that such organic molecules could be sticky and facilitate the formation of pebbles larger than millimeters in size (Lodders, 2004).

Both pebble accretion (in the Hill regime) and radial drift depend on the Stokes number of the pebbles rather than on their physical sizes. The pebble Stokes number is calculated from the radius  $R$  and material density  $\rho_\bullet$  of the pebbles through the relation

$$St = \sqrt{2\pi} \frac{R \rho_\bullet}{\Sigma_g} = \sqrt{2\pi} \frac{3\pi v R \rho_\bullet}{\dot{M}_g}. \quad (16)$$

This yields the pebble size for a given value of  $St/\alpha$  as

$$\begin{aligned} R &= \frac{St}{\alpha} \frac{\dot{M}_g}{\sqrt{2\pi} 3\pi c_s H \rho_\bullet} \\ &= 1.1 \text{ mm} \left( \frac{St}{\alpha} \right) \left( \frac{\dot{M}_g}{10^{-8} M_\odot \text{ yr}^{-1}} \right) \left( \frac{c_{s1}}{6.5 \times 10^2 \text{ m s}^{-1}} \right)^{-2} \\ &\quad \times \left( \frac{\rho_\bullet}{10^3 \text{ kg m}^{-3}} \right)^{-1} \left( \frac{r}{10 \text{ AU}} \right)^{\zeta-3/2}. \end{aligned} \quad (17)$$

In Section 3 we adopt a protoplanetary disc evolution model where the gas accretion rate drops from  $10^{-7} M_{\odot} \text{ yr}^{-1}$  to  $10^{-8} M_{\odot} \text{ yr}^{-1}$  over three million years. This gives a typical pebble size of mm-cm in the 5–20 AU region, for  $\text{St}/\alpha = 1$ , which corresponds well to the sizes of pebbles whose growth is stuck at the bouncing barrier (Zsom et al., 2010; Birnstiel et al., 2012).

The fragmentation barrier is reached when the collision speed driven by the turbulent gas motion,  $v_c = \sqrt{3\alpha_v \text{St} c_s}$  (Ormel & Cuzzi, 2007), equals an assumed fragmentation speed,  $v_f$  (Birnstiel et al., 2012). Here  $\alpha_v$  is the turbulent viscosity; we discuss its value and connection to the global disc accretion coefficient  $\alpha$  in Section 2.6. The turbulent collision speed results in a limiting Stokes number

$$\text{St} = \frac{1}{3} \alpha_v^{-1} \left( \frac{v_f}{c_s} \right)^2 = 0.003 \left( \frac{\alpha_v}{10^{-4}} \right)^{-1} \times \left( \frac{v_f}{1 \text{ m s}^{-1}} \right)^2 \left( \frac{c_{s1}}{6.5 \times 10^2 \text{ m s}^{-1}} \right)^{-2} \left( \frac{r}{10 \text{ AU}} \right)^{\zeta}. \quad (18)$$

The fragmentation barrier thus lies at a Stokes number that is (a) independent of the mass accretion rate onto the star and (b) only weakly dependent on the distance from the star.

The small pebbles stuck at the bouncing or fragmentation barrier have radial speeds that are approximately the same as the radial gas accretion speed. This results in a pebble-to-gas flux ratio  $\xi \approx Z$ , where  $Z$  is the overall metallicity of the protoplanetary disc, and hence a similar depletion time of the gaseous and solid components of the protoplanetary disc. We will therefore, for simplicity, consider  $\text{St} = \alpha$  in our models, as this choice agrees both with the bouncing and fragmentation barriers and with observations that show that pebbles of mm-cm sizes remain present in protoplanetary discs over a wide range of ages (Pérez et al., 2012; Huang et al., 2018). Choosing a larger value of  $\text{St}/\alpha$  would correspond to larger pebbles, more in agreement with pebble growth limited only by the radial drift (Birnstiel et al., 2012; Lambrechts & Johansen, 2014). Such large pebbles would lead to high pebble accretion rates, but would drain out of the protoplanetary disc on a shorter time-scale than the gas accretion time-scale (Lin et al., 2018), adding significant complication in modelling the divergent evolution of gas and pebbles.

## 2.5. Analytical core growth track

Using equation (1) for the core growth rate and equation (3) for the migration rate, we can now formulate the differential equation for the growth track  $M(r)$ ,

$$\frac{dM}{dr} = \frac{\dot{M}}{\dot{r}} = - \frac{\xi}{(2/3)(\text{St}/\alpha)\chi + 1} \frac{2(\text{St}/0.1)^{2/3} M_{\star} (3M_{\star})^{-2/3}}{k_{\text{mig}} G c_{s1}^{-2} \text{AU}^{-\zeta}} \times r^{-\zeta} M^{-1/3}. \quad (19)$$

The solution is found by separation of variables,

$$M^{4/3} - M_0^{4/3} = - \frac{(4/3)\xi}{(2/3)(\text{St}/\alpha)\chi + 1} \frac{2(\text{St}/0.1)^{2/3} M_{\star} (3M_{\star})^{-2/3}}{k_{\text{mig}} G c_{s1}^{-2} \text{AU}^{-\zeta}} \times \frac{1}{1-\zeta} (r^{1-\zeta} - r_0^{1-\zeta}). \quad (20)$$

Here  $M_0$  and  $r_0$  are the starting mass and starting location of the protoplanet, respectively. We can now divide the equation by its solution at  $r = 0$ ,  $M(0) = M_{\text{max}}$ , to obtain

$$\frac{M^{4/3} - M_0^{4/3}}{M_{\text{max}}^{4/3} - M_0^{4/3}} = 1 - \left( \frac{r}{r_0} \right)^{1-\zeta}. \quad (21)$$

The “maximum mass” reached at  $r = 0$  for  $\zeta < 1$  is given by

$$M_{\text{max}}^{4/3} = M_0^{4/3} + \frac{(4/3)\xi}{(2/3)(\text{St}/\alpha)\chi + 1} \frac{2(\text{St}/0.1)^{2/3} M_{\star} (3M_{\star})^{-2/3}}{k_{\text{mig}} G c_{s1}^{-2} \text{AU}^{-\zeta}} \times \frac{r_0^{1-\zeta}}{1-\zeta}. \quad (22)$$

For  $\zeta > 1$ , the aspect ratio  $H/r$  increases when approaching the star (equation 6) and migration is stalled by the high temperature in the inner regions of the protoplanetary disc. The protoplanet therefore never reaches  $r = 0$  in that case. We can reformulate equation (22) as a scaling law for  $M_{\text{max}}$  in the limit  $M_{\text{max}} \gg M_0$ ,

$$M_{\text{max}} = 11.7 M_{\text{E}} \frac{(\text{St}/0.01)^{1/2}}{\{[(2/3)(\text{St}/\alpha)\chi + 1]/2.9\}^{3/4}} \left( \frac{\xi}{0.01} \right)^{3/4} \times \left( \frac{M_{\star}}{M_{\odot}} \right)^{1/4} \left( \frac{k_{\text{mig}}}{4.42} \right)^{-3/4} \left( \frac{c_{s1}}{6.5 \times 10^2 \text{ m s}^{-1}} \right)^{3/2} \times \left( \frac{1-\zeta}{4/7} \right)^{-1} \left( \frac{r_0}{25 \text{ AU}} \right)^{(3/4)(1-\zeta)}. \quad (23)$$

We see here how  $\xi$ , which sets the pebble accretion rate, and  $k_{\text{mig}}$ , which sets the migration rate, pull the maximum mass in opposite directions at an exactly equal power index. Any reduction in the pebble accretion rate, e.g. from 3-D accretion if the pebble scale-height is larger than 10% of the gas scale-height in equation (2), will act in similar way as a reduction in  $\xi$  to reduce  $M_{\text{max}}$ . We assumed in the derivations above that  $k_{\text{mig}}$  is a constant. This assumption may break down in the inner, viscously heated regions of the protoplanetary disc (typically interior of 1 AU for nominal accretion rates and disc masses) where the positive corotation torque can slow down or reverse migration (Bitsch & Johansen, 2016; Brasser et al., 2017). We note also that the weak scaling with  $M_{\star}^{1/4}$  in equation (23) does not take into account that  $c_{s1}$  depends on the luminosity, and hence on the mass, of the star<sup>2</sup>.

We finally obtain the shape of the growth track,  $r(M)$ , from equation (21),

$$r(M) = r_0 \left( 1 - \frac{M^{4/3} - M_0^{4/3}}{M_{\text{max}}^{4/3} - M_0^{4/3}} \right)^{1/(1-\zeta)}. \quad (24)$$

In Appendix A we use this expression to derive the time associated with each step in the growth track. We show analytical growth tracks in Figure 1, for pairs of values of  $\alpha = \text{St}$  and  $\xi$ . We use a disc temperature profile here with  $c_{s1} = 650 \text{ m s}^{-1}$  and  $\zeta = 3/7$ , appropriate for the outer regions of the protoplanetary disc where viscous heating is negligible (Chiang & Youdin, 2010; Bitsch et al., 2015a; Ida et al., 2016). The growth tracks start off nearly vertical (growth dominates over migration), but as the migration rate increases, eventually the growth tracks turn horizontal and reach  $M_{\text{max}}$  after migrating to  $r = 0$ . Type I migration is truly a tough opponent for the planetary core to overcome.

<sup>2</sup> Assuming that the luminosity of the host star has a power-law dependence on the stellar mass,  $L_{\star} \propto M_{\star}^p$ , yields a temperature at 1 AU that scales as  $T_1 \propto L_{\star}^{2/7} M_{\star}^{-1/7} \propto M_{\star}^{(2p-1)/7}$  (Ida et al., 2016) and hence  $c_{s1} \propto M_{\star}^{(2p-1)/14}$ . That gives a combined mass-dependence of equation (23) as  $M_{\text{max}} \propto M_{\star}^{1/4 + (3p-3/2)/14}$ , which is close to linear for  $p = 3$ .

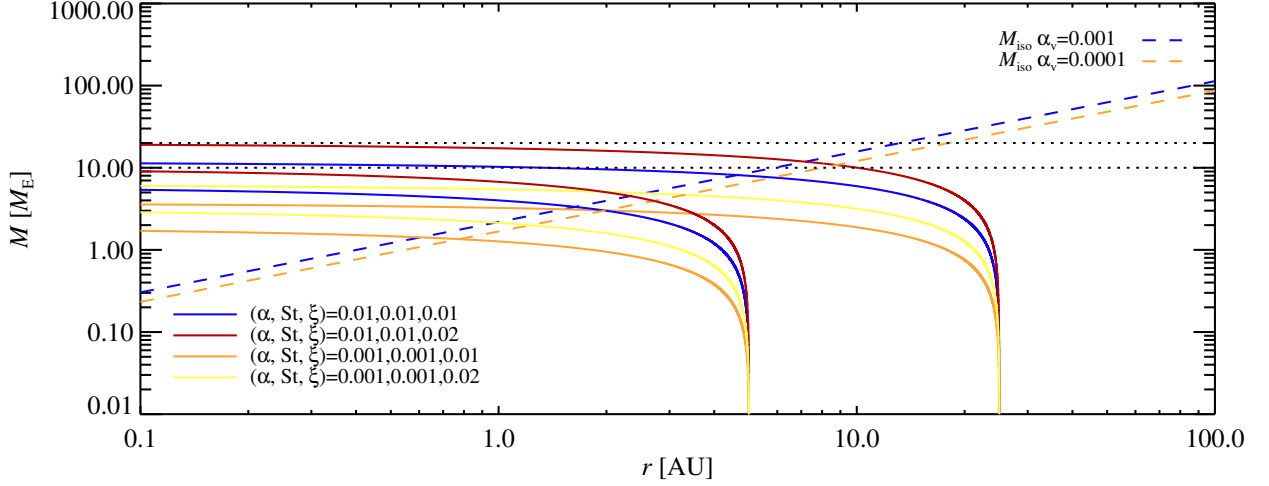


**Fig. 1.** Analytical growth tracks of planetary cores for four combinations of the accretion viscosity  $\alpha$ , the pebble Stokes number  $St$  (set to be equal to  $\alpha$ ) and the ratio of radial pebble-to-gas flux rates  $\xi$ . Protoplanets are started at either 5 AU or 25 AU and with a starting mass of  $0.01 M_E$ . The pebble isolation mass is indicated for two values of the turbulent viscosity  $\alpha_v$ , assumed here to be 0.1 times the accretion viscosity  $\alpha$ . The proportionality between the migration rate and the mass results in all growth tracks turning nearly horizontal before reaching their maximal mass at  $r = 0$ .

## 2.6. Pebble isolation mass

The core growth stage ends as the planetary core reaches the pebble isolation mass. Here the protoplanet's gravity perturbs the gas flow enough to form a plateau of Keplerian motion on the exterior side of the orbit, trapping the migrating pebbles there. The lack of heating by infalling pebbles then allows the gas to decrease its entropy by radiative heat loss and contract slowly to accrete a growing envelope around the core (Lambrechts et al., 2014). In Bitsch et al. (2018b) the pebble isolation mass was fitted to 3-D simulations by the expression

$$M_{\text{iso}} = 25 M_E \left[ \frac{H/r}{0.05} \right]^3 \left[ 0.34 \left( \frac{\log(\alpha_3)}{\log(\alpha_v)} \right)^4 + 0.66 \right] \times \left[ 1 - \frac{\partial \ln P / \partial \ln r + 2.5}{6} \right]. \quad (25)$$

Here  $\alpha_3 = 10^{-3}$  is a constant and  $\alpha_v$  is the turbulent viscosity, which we distinguish in this paper from the  $\alpha$ -value of the mass accretion rate of equation (7), as the latter may be driven by disc winds at a weak level of actual turbulence (Bai & Stone, 2013; Béthune et al., 2017). Dürmann & Kley (2015) showed that the gas flow through the protoplanetary disc achieves a constant rate through a planetary gap and that the migration rate is not dependent on the global gas flow. We therefore here assume that the global gas speed also does not affect gap formation and use  $\alpha_v = 0.1\alpha$  to calculate the pebble isolation mass in equation (25) (see Armitage et al., 2013; Hasegawa et al., 2017, for a discussion of this distinction). We motivate our usage of  $\alpha_v$  in defining the pebble isolation mass by noting that the gas speed driven by the turbulent viscosity over the length-scale of the gap, assumed to be the gas scale-height  $H$ , is

$$u_v \sim \frac{v}{H} \sim (H/r)^{-1} u_r, \quad (26)$$

where  $u_r$  is the global gas accretion speed. Hence turbulent viscosity is expected to be a factor  $(H/r)^{-1}$  times more effective

than the global gas accretion speed at counteracting gap formation. However, we emphasize that Dürmann & Kley (2015) did not distinguish between the  $\alpha$  measuring disc accretion and the  $\alpha_v$  measuring turbulent viscosity. Future studies are needed to assess the effect of the global gas accretion speed, here parameterised through  $\alpha$ , on gap formation and pebble isolation mass.

The isolation mass for the two considered values of  $\alpha_v$  is overplotted in Figure 1. The pebble isolation mass is increased over the expression given in equation (25) for small pebbles or strong particle turbulence (Bitsch et al., 2018b; Ataiee et al., 2018); we ignore such effects here since we work in the limit of weak turbulence and since even small pebbles of  $St = 0.01$  are easily trapped at the outer edge of the gap.

## 2.7. Reaching the pebble isolation mass

One can derive analytically the location where the protoplanet growth track crosses the pebble isolation mass. The pebble isolation mass changes as  $r$  decreases from its initial  $r_0$ . Scaling equation (25) from the starting position of the growth track,  $r_0$ , we obtain the expression

$$M_{\text{iso}}(r) = M_{\text{iso},0} \left( \frac{r}{r_0} \right)^{(3/2)(1-\xi)}. \quad (27)$$

Here  $M_{\text{iso},0}$  is the isolation mass at  $r = r_0$ . In the limit  $M \gg M_0$  the protoplanet therefore reaches pebble isolation mass at  $r = r_{\text{iso}}$  when

$$M_{\text{iso}}^{4/3} = M_{\text{iso},0}^{4/3} \left( \frac{r_{\text{iso}}}{r_0} \right)^{2(1-\xi)} = M_{\text{max}}^{4/3} \left[ 1 - \left( \frac{r_{\text{iso}}}{r_0} \right)^{1-\xi} \right]. \quad (28)$$

This equation forms a second order polynomial,

$$\left( \frac{M_{\text{iso},0}}{M_{\text{max}}} \right)^{4/3} X^2 + X - 1 = 0, \quad (29)$$

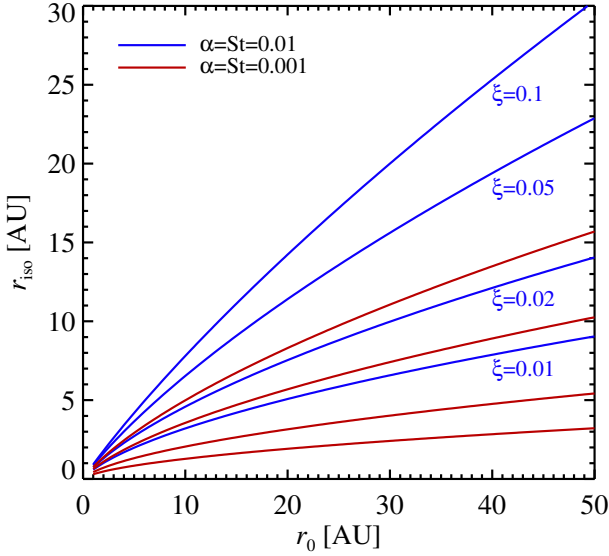


**Fig. 2.** Radial location of reaching the pebble isolation mass,  $r_{\text{iso}}$ , as a function of the starting position in the disc,  $r_0$ , for different values of the pebble-to-gas flux ratio  $\xi$ . For low values of  $\xi$ , reaching the pebble isolation mass in the 5–10 AU region requires migration over tens of AU. Nearly in-situ assembly of a planetary core is possible when the pebble-to-gas flux ratio  $\xi \gtrsim 0.05 - 0.1$ .

with  $X = (r_{\text{iso}}/r_0)^{1-\zeta}$  or  $\Delta r_{\text{iso}} = r_0 - r_{\text{iso}} = [1 - X^{1/(1-\zeta)}]r_0$ . The positive solution to the polynomial is

$$X = \frac{\sqrt{1 + 4A} - 1}{2A}, \quad (30)$$

where  $A = (M_{\text{iso},0}/M_{\text{max}})^{4/3}$ . Note that a solution exists for all  $A$ , i.e. the pebble isolation mass is reached for all starting positions  $r_0$ . That is due to the steeply falling pebble isolation mass with decreasing distance, in the passively irradiated case. Our results generally do not apply to the viscously heated interior regions of the protoplanetary disc where  $\zeta$  increases and the aspect ratio becomes relatively constant (Bitsch et al., 2015a; Ida et al., 2016; Brasser et al., 2017).

In the limit  $A \gg 1$ , corresponding to  $r_0 \gg r_{\text{iso}}$  through equation (28), equation (30) has the limiting solution

$$X = A^{-1/2} \quad (31)$$

and hence the isolation mass is reached at radius

$$r_{\text{iso}}/r_0 = A^{-(1/2)[1/(1-\zeta)]}. \quad (32)$$

We can furthermore make use of  $M_{\text{iso},0} \propto r_0^{(3/2)(1-\zeta)}$  and  $M_{\text{max}} \propto r_0^{(3/4)(1-\zeta)}$  to infer  $A = (M_{\text{iso},0}/M_{\text{max}})^{4/3} \propto r_0^{1-\zeta}$ . That gives now the simple relation

$$r_{\text{iso}} \propto r_0^{1/2}. \quad (33)$$

The length over which the protoplanet migrates before reaching pebble isolation mass is therefore a steeply increasing function of the starting position. In the same limit ( $r_0 \gg r_{\text{iso}}$ ) the reached pebble isolation mass becomes simply  $M_{\text{iso}} = M_{\text{max}}$ , by inserting  $r_{\text{iso}}/r_0$  in equation (28). This simple result arises because the growth track turns nearly horizontal after a significant migration

distance and hence the core is close to its maximum mass  $M_{\text{max}}$  when it finally reaches pebble isolation mass.

In Figure 2 we plot the calculated distance of reaching isolation mass,  $r_{\text{iso}}$ , as a function of the starting position,  $r_0$ , for different values of  $\alpha = \text{St}$  and  $\xi$ . The distance is obtained from the full solution of equation (29). For a core to reach isolation mass in the 5–10 AU region, the protoplanet must generally start beyond 20 AU, for nominal values of  $\xi = 0.01 - 0.02$ . Nearly in-situ core assembly by pebble accretion requires much higher values of  $\xi \gtrsim 0.05 - 0.1$ .

### 3. Growth tracks including gas accretion

We now include the effect of gap formation and gas accretion on planetary growth tracks. We turn to numerical integration, since the reduction of the migration rate and gas accretion rate by gap formation render the governing equations much more complex.

#### 3.1. Type I migration and gap depth

Kanagawa et al. (2018) performed a suite of 2-D simulations to measure the torque on embedded planets of a wide range of masses. They found that the torque is well-described by the classical Type I torque, which gives rise to the migration rate expression given in equation (3), multiplied by the relative gap height,

$$\Gamma = -c_{\text{mig}} \Gamma_0 \frac{\Sigma_{\text{gap}}}{\Sigma_{\text{g}}}. \quad (34)$$

Here  $c_{\text{mig}} = k_{\text{mig}}/2$  is the torque prefactor,  $\Sigma_{\text{gap}}$  is the surface density in the gap,  $\Sigma_{\text{g}}$  is the unperturbed surface density and  $\Gamma_0 (\propto M^2)$  is the natural torque scaling. The surface density at the bottom of the gap is fitted well by the expression (Duffell & MacFadyen, 2013; Fung et al., 2014; Kanagawa et al., 2015; Fung & Chiang, 2016)

$$\frac{\Sigma_{\text{gap}}}{\Sigma_{\text{g}}} = \frac{1}{1 + 0.04K}, \quad (35)$$

where

$$K = \left(\frac{M}{M_{\star}}\right)^2 \left(\frac{H}{r}\right)^{-5} \alpha_{\text{v}}^{-1}. \quad (36)$$

This implies that the migration rate,  $\dot{r} = 2\Gamma/(Mv_{\text{K}})$ , falls as  $1/M$  above the gap transition mass  $M_{\text{gap}}$  (defined as the mass for which  $K = 1/0.04$ ). The gap transition mass and the pebble isolation mass are actually closely related concepts. While the gap transition mass measures the mass required to make a relative gap depth of 0.5, the pebble isolation mass measures the first appearance of a point of zero pressure gradient at the outside of the planetary gap. The latter criterion is slightly easier to fulfill, as a relative gap height of around 0.85 is sufficient to invert the pressure gradient in the simulations of Bitsch et al. (2018b) (we inferred this gap depth from their Figure A.1).

To check the robustness of the relative gap height needed for pebble isolation, we performed additional 1-D simulations of an accretion disc with an embedded planet, varying the turbulent viscosity. The torque from the planet was mimicked using the torque profile of D’Angelo & Lubow (2010), based on their 3-D simulations. The simulations were run until the gap depth reached equilibrium between the gap-opening torque and the viscous momentum transport ( $10^3, 10^4, 10^5$  yr for  $\alpha_{\text{v}} = 10^{-2}, 10^{-3}, 10^{-4}$ , respectively). The results are shown in Figure 3 and confirm that the pebble isolation mass is reached at a relative gap

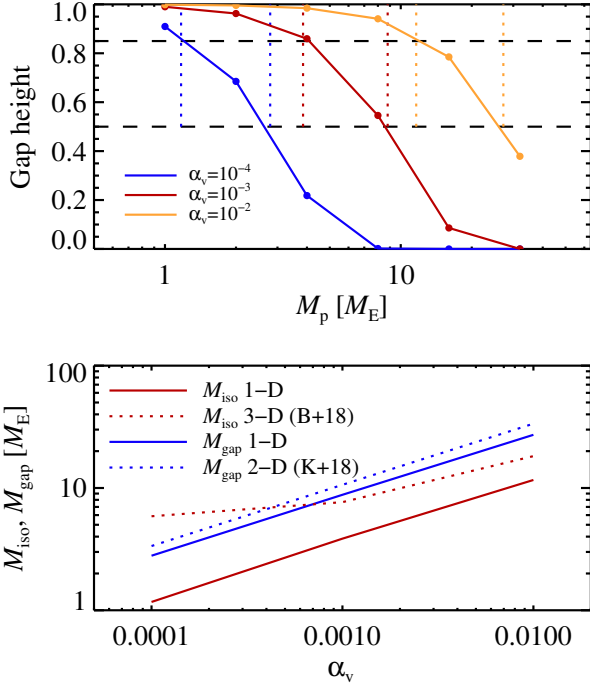


**Fig. 3.** The results of 1-D simulations of an accretion disc with an embedded planet whose torque on the gas is based on the parametrisations of D’Angelo & Lubow (2010). The top panel shows the equilibrium gap height as a function of the planetary mass, for three values of the viscous  $\alpha_v$ . The dashed lines mark the 50% gap depth and the 85% gap depth, the latter approximately corresponding to the pebble isolation mass. The bottom panel shows the pebble isolation mass ( $M_{iso}$ ) and the gap transition mass ( $M_{gap}$ ) as a function of  $\alpha_v$ . We find generally that  $M_{gap} \approx 2.3M_{iso}$ . The measured gap transition mass corresponds well to the 2-D simulations Kanagawa et al. (2018), while the measured pebble isolation mass is about a factor two lower than reported in Bitsch et al. (2018b) and displays a more consistent drop with lower  $\alpha_v$ .

height of 0.85. We find a general scaling that the gap transition mass, i.e. the mass of 50% gap depth, is 2.3 times the pebble isolation mass. The measured gap transition mass agrees well with the gap depth scaling in equations (35) and (36), particularly that the gap transition mass scales with the square root of  $\alpha_v$ .

We nevertheless encountered some discrepancy between the  $\alpha_v$ -dependence of the pebble isolation mass inferred from our simulations and those of Bitsch et al. (2018b). At high and medium  $\alpha_v$  ( $10^{-2}$  and  $10^{-3}$ ) our 1-D pebble isolation mass is approximately a factor two lower than the 3-D pebble isolation mass of Bitsch et al. (2018b). It is nevertheless well-known that gaps formed by a 1-D torque prescription become artificially deeper than what is found in 2-D and 3-D simulations (Hallam & Paardekooper, 2017). For low  $\alpha_v$  ( $10^{-4}$ ) the pebble isolation mass of by Bitsch et al. (2018b) furthermore showed a weak logarithmic scaling with  $\alpha_v$  (equation 25), while our 1-D pebble isolation mass maintains its proportionality to the square root of  $\alpha_v$ , similar to the scaling of the gap transition mass with  $\alpha_v$  (equations 35 and 36). This difference could be due to (1) Rossby wave instabilities triggered at the gap edge at low  $\alpha_v$  in 3-D simulations or (2) that the simulations of Bitsch et al. (2018b) were run only for 1,000 orbital time-scales at the planet position. The

2-D simulations of Ataiee et al. (2018) also show a somewhat weaker dependence of the pebble isolation mass on  $\alpha_v$  than the square root dependence that we find in Figure 3. Identifying the actual reason for the discrepancy will require a dedicated study beyond the scope of the current paper. Since we will focus in the remainder of the paper on the case  $\alpha_v = 10^{-3}$  and  $\alpha = 10^{-2}$ , we will set the pebble isolation mass according to Bitsch et al. (2018b) and the gap transition mass to 2.3 times the pebble isolation mass. This yields a modified migration equation

$$\dot{r} = \frac{\dot{r}_I}{1 + [M/(2.3M_{iso})]^2}, \quad (37)$$

where  $\dot{r}_I$  is the classical Type I migration rate and  $M_{iso}$  is the pebble isolation mass given in equation (25).

Reaching first the pebble isolation mass and shortly after the gap transition mass thus signify three important mile-stones for the growth of a protoplanet: (a) the end of the accretion of pebbles, (b) the beginning of gas contraction and (c) the transition to a slow-down in the migration caused by the deepening gap.

### 3.2. Gas accretion

The gas accretion rate of a protoplanet embedded in a protoplanetary disc is highly uncertain. Even the term *accretion* is, in our opinion, slightly misleading, as the mass increase takes place in the form of a contraction of the envelope due to entropy reduction by radiative heat loss. Klahr & Kley (2006) demonstrated that the circumplanetary disc formed in some isothermal simulations is replaced by a hot, hydrostatic gas blob in simulations including compressive heating and radiative transfer. Ikoma et al. (2000) performed 1-D simulations of the envelope contraction and found run-away contraction where the energy loss, and hence contraction rate, is accelerated at higher envelope masses. D’Angelo & Bodenheimer (2013) presented extensive simulations of the gas contraction onto low-mass cores and found, as in earlier 1-D work, that the contraction is accelerated at higher core mass (the same trend was observed in Lambrechts & Lega, 2017). Lambrechts et al. (2018) measured the gas contraction rate in hydrodynamical simulations with radiative transfer, for planetary cores of up to Jupiter-mass. They found that the accretion rate is orders of magnitude lower than the mass flux passing through the Hill radius, as most of this gas is transported out again on horse-shoe orbits and more complex streamlines.

We use here the gas accretion prescription proposed in Ida et al. (2018), taking into account both the Kelvin-Helmholtz-like contraction of the envelope and the feeding of gas from the protoplanetary disc into the Hill sphere of the protoplanet. The contraction of the gaseous envelope is assumed to commence after the core reaches pebble isolation mass, at a rate motivated by Ikoma et al. (2000),

$$\left(\frac{dM}{dt}\right)_{KH} = 10^{-5} M_E \text{ yr}^{-1} \left(\frac{M}{10M_E}\right)^4 \left(\frac{\kappa}{0.1 \text{ m}^2 \text{ kg}^{-1}}\right)^{-1}. \quad (38)$$

Here  $\kappa$  is the opacity of the envelope, which we discuss further below. This accretion rate will become larger than what the protoplanetary disc can supply for high planetary masses. Tanigawa & Tanaka (2016) used isothermal, global simulations to demonstrate that gas enters the Hill sphere at a rate

$$\begin{aligned} \left(\frac{dM}{dt}\right)_{disc} &= \frac{0.29}{3\pi} \left(\frac{H}{r}\right)^{-4} \left(\frac{M}{M_\star}\right)^{4/3} \frac{\dot{M}_g}{\alpha} \frac{\Sigma_{gap}}{\Sigma_g} \\ &= 1.5 \times 10^{-3} M_E \text{ yr}^{-1} \left(\frac{H/r}{0.05}\right)^{-4} \left(\frac{M}{10M_E}\right)^{4/3} \end{aligned}$$

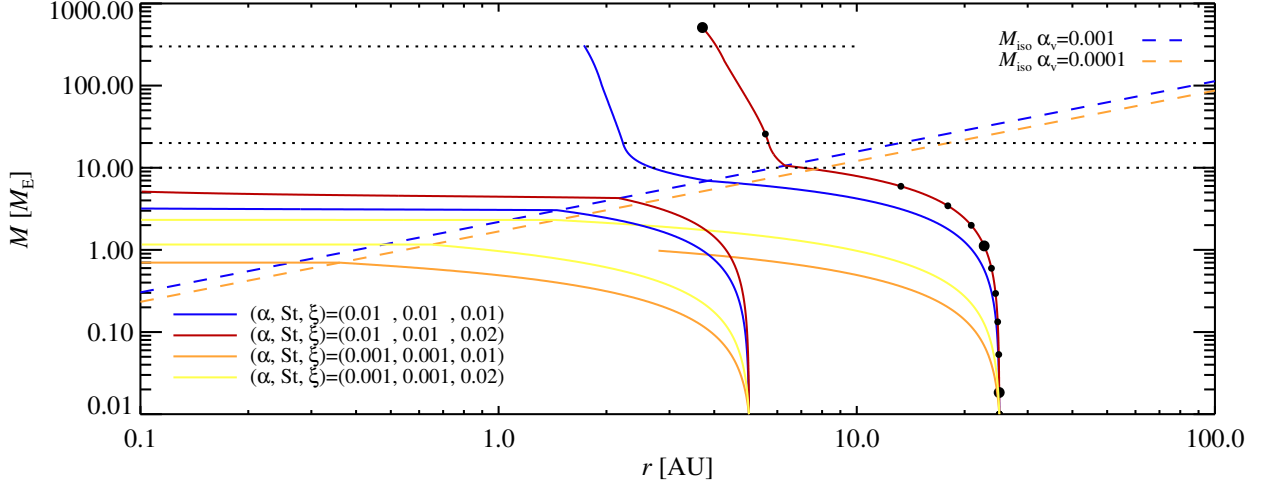


**Fig. 4.** Numerically integrated growth tracks for core accretion to the pebble isolation mass followed by gas accretion. We start the protoplanets at a mass of  $M_0 = 0.01 M_E$  at  $t_0 = 0.9$  Myr (except for the  $\alpha = St = 0.01$  growth track starting from 25 AU, which we start at  $t_0 = 0.3$  Myr) in a protoplanetary disc that evolves over a total time of 3 Myr. The dots indicate the time for the growth track that successfully forms a Jupiter analogue (small dots are separated by 0.2 Myr, large dots indicate a time of 3, 2 and 1 Myr). We use a migration model where the migration rate is reduced by multiplication with the gap depth, following Kanagawa et al. (2018). The migration rate is therefore inversely proportional to the planet mass beyond the pebble isolation mass. This results in gas accretion over a few astronomical units of migration.

$$\times \left( \frac{\alpha}{0.01} \right)^{-1} \left( \frac{\dot{M}_g}{10^{-8} M_\odot \text{ yr}^{-1}} \right) \frac{1}{1 + (M/M_{\text{gap}})^2}. \quad (39)$$

This equation is derived in the companion paper by Ida et al. (2018) – we note here that the simpler form,  $(dM/dt)_{\text{disc}} \propto R_H^2 \Omega \Sigma_{\text{gap}} (R_H/H)^2$ , shows that the equation can be decomposed into the full flux into the Hill sphere multiplied by the squared ratio of the Hill radius to the scale-height. The latter reflect the increasing ability of the protoplanet to accrete the gas streamlines that enter the Hill radius as the mass increases (Tanigawa & Tanaka, 2016).

The prefactor in equation (39) can be converted to solar units to compare with the disc accretion rate,  $1.5 \times 10^{-3} M_E \text{ yr}^{-1} \approx 4.5 \times 10^{-9} M_\odot \text{ yr}^{-1}$ . If the planet contracts rapidly enough to absorb the entire gas flow into the Hill radius, then we must therefore limit the accretion rate to the global gas accretion rate (see Lubow & D’Angelo, 2006, for a discussion of this limit). We therefore set the gas accretion rate of the planet equal to

$$\left( \frac{dM}{dt} \right)_g = \min \left[ \left( \frac{dM}{dt} \right)_{\text{KH}}, \left( \frac{dM}{dt} \right)_{\text{disc}}, \dot{M}_g \right]. \quad (40)$$

Ikoma et al. (2000) found that the Kelvin-Helmholtz gas accretion rate increases inversely proportionally to the opacity  $\kappa$  (equation 38). Bitsch & Johansen (2016) calculated an opacity of micron-sized ice particles in the range  $0.01 - 0.1 \text{ m}^2 \text{ kg}^{-1}$ . For core accretion by pebble accretion, we expect that the accreted gas will be completely pebble-free beyond the pebble isolation mass (Lambrechts et al., 2014). Small dust can nevertheless pass the planet barrier together with the accreted gas, constituting maybe 10% of the total content of solids. That gives a nominal opacity in the range  $0.001 - 0.01 \text{ m}^2 \text{ kg}^{-1}$ . The opacity could be even lower if the grains in the envelope coagulate and sediment (Mordasini, 2014). We adopt here a standard opacity value of  $\kappa = 0.005 \text{ m}^2 \text{ kg}^{-1}$ .

### 3.3. Protoplanetary disc model

The growth rates reported in Ikoma et al. (2000) were measured at a single value of the gas surface density and gas temperature at the outer boundary. Hence the dependence of the accretion rates on the gas surface density and temperature is not known. If the gas contraction is indeed limited by the ability of the envelope to cool, then the outer boundary condition may not matter much (as found by Piso & Youdin, 2014; Lee & Chiang, 2015). This, in turn, implies that mass accretion wins more easily over migration when the gas disc is depleted compared to the primordial value, since the initial gas accretion rate is relatively unaffected by the protoplanetary disc surface density, while the migration rate is proportional to the surface density<sup>3</sup>.

The dependence of the migration rate on the gas surface density, combined with the non-dependence of the Kelvin-Helmholtz contraction rate on the surface density, therefore necessitates a specific disc evolution model to integrate the growth tracks. We use a standard viscous accretion disc model where  $\dot{M}_g$  evolves from  $10^{-7} M_\odot \text{ yr}^{-1}$  to  $10^{-8} M_\odot \text{ yr}^{-1}$  over 3 Myr. Following Hartmann et al. (1998), the accretion rate onto the star evolves as

$$\dot{M}_g(t) = \dot{M}_0 \left[ \frac{t}{t_s} + 1 \right]^{-(5/2-\gamma)/(2-\gamma)}, \quad (41)$$

where  $\gamma$  is the power-law index of the turbulent viscosity,  $\nu \propto r^\gamma$ , and the characteristic time-scale,  $t_s$ , is

$$t_s = \frac{1}{3(2-\gamma)^2} \frac{R_1^2}{\nu_1}. \quad (42)$$

Here  $R_1$  is the initial characteristic disc size and  $\nu_1$  is the value of the viscosity at that radius. Knowing the temperature power

<sup>3</sup> The reduced migration rate at low gas column densities is an important component of the model of super-Earth formation in depleted gas discs presented in Lee & Chiang (2016).

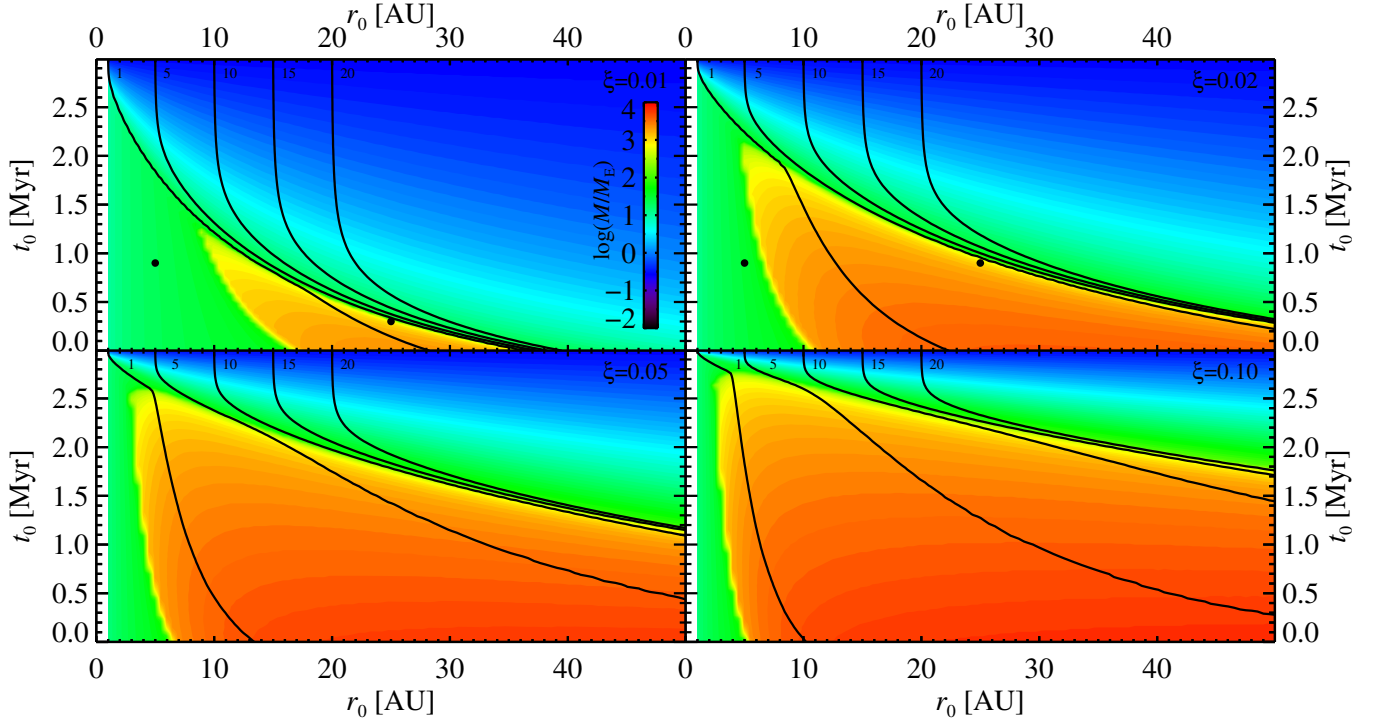


**Fig. 5.** Growth maps showing final masses (colors) and selected final positions (black contours) of protoplanets starting at 1 to 50 AU distance from the star after between 0 and 3 Myr of disc evolution. The four panels show the results for different values of the pebble-to-gas flux ratio  $\xi$ . The starting points of the selected growth tracks from Figure 4 are indicated with dots. The cores of cold gas giants akin to Jupiter and Saturn start their assembly here in the 20–30 AU region for nominal values of  $\xi = 0.01 - 0.02$ . Higher values of  $\xi$  allow core assembly closer to the central star, starting in the 10–15 AU region.

law index  $\zeta$  results in  $\gamma = 3/2 - \zeta$  ( $= 15/14$  for  $\zeta = 3/7$ ). We proceed by choosing  $R_1$  to yield the desired starting and ending mass accretion rate over an assumed disc life-time of 3 Myr.

We take into account in the numerical simulations that the pebble accretion rate is lowered when the pebble scale-height is higher than the pebble accretion radius, following the method described in Johansen et al. (2015). Johansen & Klahr (2005) demonstrated in MHD simulations that the turbulent viscosity  $\alpha_v$  and the turbulent diffusion coefficient  $\delta$  are approximately equal; we therefore for simplicity assume  $\delta = \alpha_v$  in our simulations.

### 3.4. Growth tracks with gas accretion

The integration of the growth track bundles from Figure 1 including gas accretion are shown in Figure 4. We start the growth tracks at  $t_0 = 0.9$  Myr and integrate until the disc is assumed to dissipate after  $t = 3$  Myr. To demonstrate the effect of the starting time, we start one growth track (with  $\alpha = \text{St} = 0.01$  and  $\xi = 0.01$  starting at  $r_0 = 25$  AU) at  $t_0 = 0.3$  Myr. The core growth tracks before reaching pebble isolation mass are relatively unaffected by the slow-down of the migration rate towards the gap transition mass (and follows the analytical solution that we derived in Section 2, even when we include here that the initial pebble accretion is reduced in 3-D). However, after reaching the pebble isolation mass, the two growth tracks starting at 25 AU with  $\alpha = \text{St} = 0.01$  turn quickly upwards, as the migration rate falls inversely proportional to the planetary mass. This results in gas accretion length scales that are much shorter than the core accretion length scale. In contrast to this, the growth tracks starting at 5 AU reach an isolation mass of  $M_{\text{iso}} \sim 1 \dots 5 M_{\text{E}}$ . At those core

masses, Kelvin-Helmholtz contraction is very slow, according to equation (38), and these planets migrate towards the star with little success at accreting gas.

In Figure 5 we show the final positions of protoplanets starting at 1 to 50 AU distance from the star in the protoplanetary disc and starting times between 0 and 3 Myr, for four values of the pebble-to-gas flux ratio  $\xi$ . The slow-down of migration in the gas accretion phase allows more space for migration during the core accretion stage, hence we can form gas giants at a lower pebble accretion rate than in Bitsch et al. (2015b). For nominal pebble-to-gas flux ratios of  $\xi = 0.01 - 0.02$ , the cores of cold gas giants with final orbits in the 5–10 AU region (analogues of Jupiter and Saturn in the Solar System) start their assembly much further out, in the 20–30 AU region. Shorter migration distances, with starting locations in the 10–15 AU region, are possible at higher pebble-to-gas flux ratios  $\xi = 0.05 - 0.1$ .

We find generally that our integrations produce much fewer hot and warm gas giants, with final orbits interior to 1 AU, compared to simulations that considered the traditional Type II migration (Bitsch & Johansen, 2016, 2017). This is due to the slow-down of the migration rate with the formation of a deep gap when using the Kanagawa et al. (2018) migration prescription here. Other studies have invoked photoevaporation as an effect to prevent massive planets from migrating all the way to the inner edge of the protoplanetary disc (Alexander & Pascucci, 2012; Ercolano & Rosotti, 2015); here and in Ida et al. (2018) we show that massive planets may be naturally prevented from migrating to the disc edge due to the deep gas gaps that they carve.

The core masses of our synthetic planets are nevertheless smaller than what is inferred for total content of heavy elements

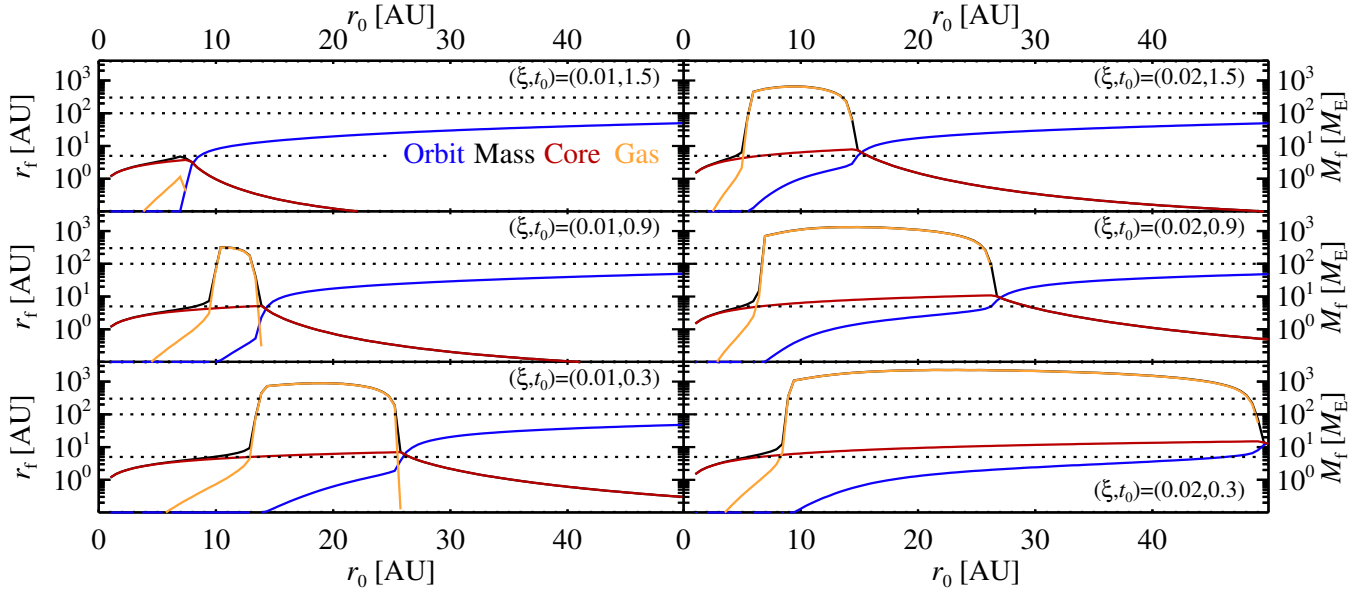


**Fig. 6.** The final orbits (left axis) and final total mass, core mass and gas (right axis) for protoplanets starting from 1 to 50 AU (bottom/top axis), at three starting different times,  $t_0=0.3, 0.9, 1.5$  Myr (bottom to top panels) and for two values of  $\xi=0.01, 0.02$  (left and right panels). The dotted lines indicate masses or orbits of 5, 100 and 300. Protoplanets starting far from the star experience both little growth and migration. As the starting position approaches the star, the core mass grows towards  $10 M_E$ , triggering rapid migration and gas accretion. However, protoplanets that start interior of 5 AU have very protracted gas accretion due to the low pebble isolation mass there. The best analogues of Jupiter, Saturn, Uranus and Neptune start their assembly in the region around 25 AU for  $\xi = 0.02$  and  $t_0 = 0.9$  Myr.

in the gas giants in the Solar System. The recent data on the gravitational field of Jupiter by the Juno satellite yield a total amount of heavy elements between  $25 M_E$  and  $45 M_E$  (Wahl et al., 2017). However, we did not include in our simulations the contribution from planetesimal pollution during the gas accretion phase. Shiraishi & Ida (2008) modelled the pollution by late planetesimal infall numerically and found accretion of up to  $10 M_E$  of additional planetesimals, bringing the total amount of heavy elements more in line with observations.

The final orbits and masses for three selected starting times are shown in Figure 6. One sees how the outcome of planet formation can be broadly divided into three categories. Protoplanets starting their growth far from the star experience both little growth and little migration and end as ice planets with masses broadly between  $0.1$  and  $2 M_E$  (as also found by Bitsch et al., 2015a). As the starting position is reduced, the cores grow towards the pebble isolation mass of  $\approx 10 M_E$ . This triggers rapid gas accretion and the formation of Jupiter and Saturn analogues. The total gas mass plateaus at around  $1000 M_E$ ; this is an effect of gap formation that limits gas accretion in our gas accretion model that follows Tanigawa & Tanaka (2016). Protoplanets that start closer than approximately 5 AU of the host star have low pebble isolation masses and hence never experience gas accretion. These form analogues of the super-Earths found around many stars (Batalha et al., 2013), although we emphasize here that the mutual dynamics of trains of such migrating super-Earths, not included here, is key to understanding the final orbits and multiplicities of super-Earth-mass migrators (Izidoro et al., 2017; Matsumura et al., 2017). We also ignore here the truncation of the inner disc by the magnetospheric cavity, which may play an important role in reducing or halting migration (Lee & Chiang, 2017; Liu et al., 2017). Our model does not readily explain how to stop the accretion of gas at the mass of Saturn or

Jupiter, unless we invoke special timing of the dissipation of the gaseous protoplanetary disc. A possible solution to this problem is that the turbulent viscosity,  $\alpha_v$ , is even lower than what we have assumed and that both the pebble isolation mass and gap transition mass are lower in real protoplanetary discs. An earlier onset of gap formation would be an efficient way to limit the flow of gas to the protoplanet, through equation (39).

### 3.5. Formation of ice giants

Forming planets with core masses equivalent to those of Uranus and Neptune in 10-20 AU orbits (as is broadly consistent with the initial condition for the later planetesimal-driven migration of the giant planets Gomes et al., 2005) is possible when a protoplanet starts slightly exterior to those that end up forming gas giants. However, the parameter space for forming ice giants is quite small, since gas accretion is rapid for those core masses. If, on the other hand, the ice giants formed by giant impacts of a higher number of 5-Earth-mass cores, as explored in Izidoro et al. (2015), then the seeds of the ice giants would be allowed to form even further from the Sun and not be in such a high risk of accreting substantial amounts of gas.

### 3.6. Population synthesis

In Figure 7 we illustrate the planetary populations arising from our models by performing a population synthesis operation on the growth maps for  $\xi = 0.01$  and  $\xi = 0.02$ . We have sampled 10,000 random points in each growth map, using a logarithmic distribution of starting points and a linear distribution of starting times. We have also calculated the compositions of the planetary cores, by assuming that half of the mass of the pebbles is in the form of water ice outside of the water ice line. The water ice line

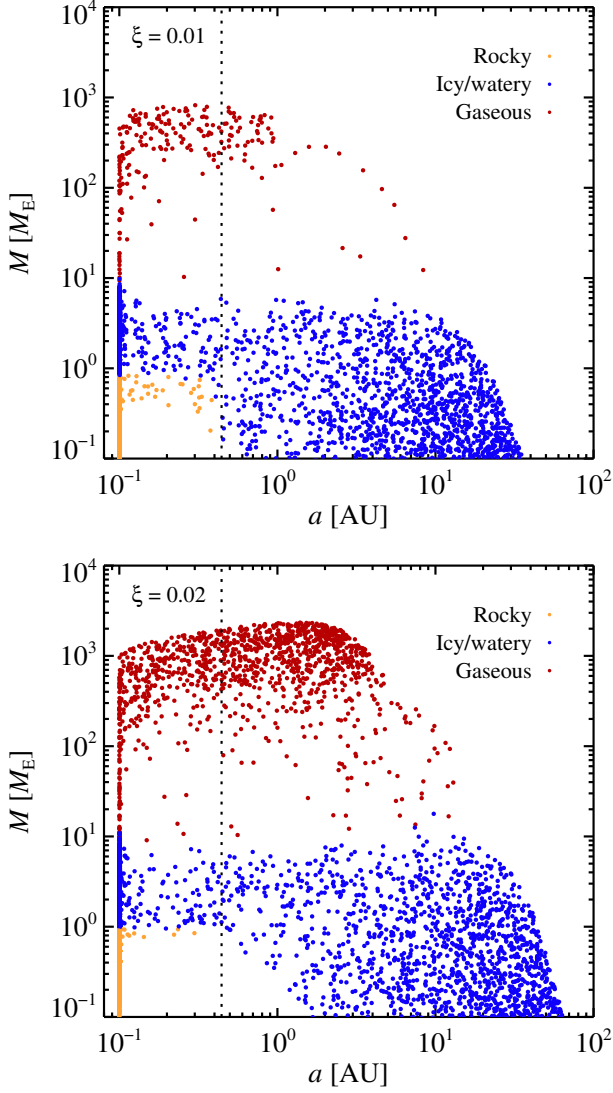


**Fig. 7.** Population synthesis of two of the growth maps shown in Figure 5. We have selected 10,000 points sampled randomly in the logarithmic starting position and the linear starting time. Core-dominated planets with an ice or water fraction of less than 25% are marked in yellow, core-dominated planets with an ice or water fraction between 25% and 50% are marked in blue and gas-dominated planets are marked in red. The water ice line is indicated by a dotted line.

is situated at around 0.45 AU in our simulations, due to the fact that we do not include viscous heating. The population synthesis demonstrates a clear dichotomy between those planets that reach the pebble isolation mass and undergo rapid gas accretion and those that stay below the pebble isolation mass. The run-away nature of early gas accretion leaves the region between 10 and 100 Earth masses relatively empty (this is known as the planet desert, see Ida & Lin, 2004).

Our pebble accretion population synthesis plots appear qualitatively similar to those presented in Bitsch & Johansen (2017) and Ndugu et al. (2018). We refer to those two papers for comparisons to the observed exoplanet populations. One notable difference is the relatively fewer gas giants that reach the inner disc edge in our simulations. This is mainly an effect of the new plan-

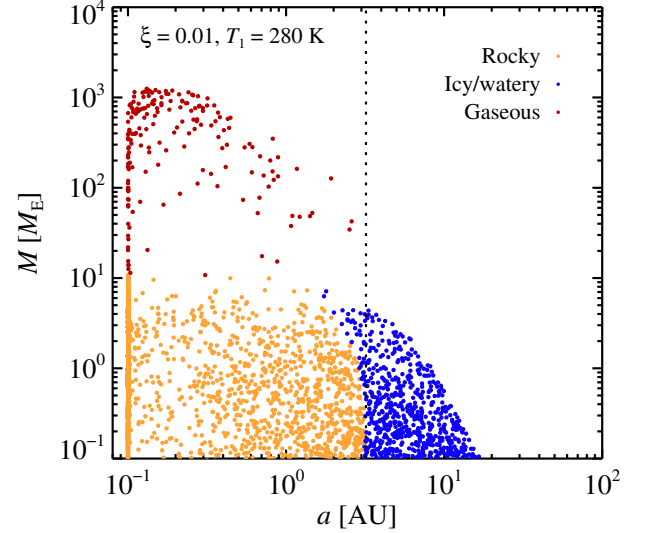


**Fig. 8.** Population synthesis plot for  $\xi = 0.01$  and a temperature of  $T_1 = 280$  K at  $r = 1$  AU. The larger aspect ratio  $H/r$ , compared to Figure 7, slows down type I migration to a degree that icy embryos formed beyond the water ice line either stay small or grow into gas giant cores. This yields mainly dry super-Earths interior of the water ice line, in agreement with constraints from exoplanet observations (Owen & Wu, 2017). However, the increased gas scale-height also slows down both pebble accretion and gas accretion, resulting in fewer gas giants in the outer regions of the protoplanetary disc.

etary migration prescription that we explore here. Comparing our results to Brügger et al. (2018) (who used a correction to the pebble sizes and fluxes of Bitsch et al., 2015b, resulting in very low pebble fluxes), we find very similar synthetic exoplanet populations, although the small-pebble model that we advocate here requires much lower pebble fluxes (and hence metallicities) to trigger the formation of gas giants in cold orbits. Chambers (2018) presented a comprehensive suite of population synthesis calculations and used the observed exoplanet populations to pin down the best set of model input parameters for the protoplanetary disc and the pebble sizes. He found best fits to the data for low diffusion coefficients ( $\sim 10^{-5}$ ), which can be understood because of the positive effect of lowering the diffusion coefficient in the initial 3-D stage of pebble accretion.

Super-Earths with final orbits within the water ice line in Figure 7 transition from dry to water-rich at a mass of approximately one Earth mass, as more massive migrators accrete a large fraction of their mass outside of the water ice line. This composition appears to be in contrast with the inferred rocky compositions of super-Earths (Owen & Wu, 2017). However, we have neglected in this paper the viscous heating that would increase the disc aspect ratio  $H/r$  in the inner regions of protoplanetary discs. An increase in the disc aspect ratio leads to lower migration rates in the inner protoplanetary disc and hence slows down the icy embryos that penetrate from beyond the ice line. The outwards migration resulting from such viscous heating will furthermore block the inwards flow of icy embryos of a certain mass range (Bitsch & Johansen, 2016).

In Figure 8 we show a population synthesis calculation on a model where the temperature at 1 AU is set to the higher value  $T_1 = 280$  K, corresponding to a sound speed of  $c_{s1} = 9.9 \times$

$10^2 \text{ m s}^{-1}$ . This temperature corresponds to the Minimum Mass Solar Nebula model of Hayashi (1981). Through equation (23) this increase in sound speed leads to a larger maximum mass, due to the slower migration speed at an increased  $H/r$ . The result is that terrestrial planets and super-Earths interior of the water ice line are now mainly rocky. Icy embryos formed exterior of the ice line either stay small, if they form late, or grow to gas giants.

In contrast to our results, Lin et al. (2018) reported that their pebble accretion models led mostly to the formation of very small cores that did not reach pebble isolation mass. This result seems to be a consequence of their large variation in the parameter  $St/\alpha$ . As shown in equation (23), a low value of  $St$  causes growth tracks to be strongly migration-dominated. An additional difference between our work and Lin et al. (2018) is that we assume that the initial gas contraction follows on the time-scale reported in Ikoma et al. (2000), which depends linearly on the opacity. Lin et al. (2018), on the other hand, consider dust-free envelopes and hence even very low-mass cores can grow to form gas giants in their models.

#### 4. Summary and discussion

In this paper we have addressed the question of how planetary growth is able to outperform migration. Type I migration likely operates at its full strength in the outer regions of the protoplanetary disc where planetary cores grow to form gas giants and ice giants, in contrast to the viscously heated inner regions of the protoplanetary disc where the positive corotation torques slow down or reverse the migration of super-Earth cores (Bitsch & Johansen, 2016; Brasser et al., 2017).

We derived analytical growth tracks for a protoplanet undergoing pebble accretion while migrating towards the star. We used these analytical expressions to derive the radial location where the growing core reaches the pebble isolation mass. Our analytical growth tracks demonstrate that protoplanets undergo substantial migration during their growth towards the pebble isolation mass and that the location of reaching the pebble isolation mass increases as the square root of the starting location.

An important new ingredient in our model, compared to previous studies of pebble accretion and migration (Bitsch et al., 2015b; Matsumura et al., 2017), is the reduction of the migration torque due to the growing planetary gap (Kanagawa et al., 2018). We identify here the close connection between the 50% gap mass,  $M_{\text{gap}}$ , of Kanagawa et al. (2018) and the pebble isolation mass,  $M_{\text{iso}}$ , of Lambrechts et al. (2014). From numerical simulations of low-mass planets embedded in a 1-D model of a protoplanetary disc, we infer that  $M_{\text{gap}} \approx 2.3M_{\text{iso}}$ . Reaching first the pebble isolation mass and slightly later the gap transition mass thus signifies three important events in the growth of a protoplanet: (a) the end of the accretion of pebbles, (b) the beginning of gas contraction and (c) the transition to a slow-down in the migration caused by the deepening gap. Gas accretion can therefore take place over just a few astronomical units of migration.

We have demonstrated that protoplanets can grow to gas-giant planets in a model where pebbles are millimeter-sized and the pebble-to-gas flux ratio is in the nominal range  $\xi = 0.01 - 0.02$ , in contrast to the models of Bitsch et al. (2015b), Bitsch et al. (2018a) and Brügger et al. (2018) where pebbles were allowed to grow to the radial drift barrier. The radial drift of the millimeter-sized pebbles considered in this work is dominated by the advection with the gas accretion flow – and the gas and pebble components of the protoplanetary disc therefore

drain onto the central star on a similar time-scale. This model avoids the radial drift problem where large pebbles drift out of the protoplanetary disc on a time-scale that is much shorter than the gas accretion time-scale (Brauer et al., 2007).

Our results show that the cores of gas-giants ending in 5–10 AU orbits must generally start their assembly from planetesimals forming in the 15–30 AU region. This raises the question of why planetesimals forming at such distances would be the seeds of the gas giants. The water ice line has been demonstrated to be a preferred location for the formation of planetesimals (Ros & Johansen, 2013; Ida & Guillot, 2016; Schoonenberg & Ormel, 2017; Drążkowska & Alibert, 2017). If the ice lines of more volatile species, e.g. CO (Qi et al., 2013), are equally prone to forming planetesimals, then this may explain why the cores of the gas-giants in the Solar System started as seeds far away from the Sun and subsequently migrated to their current orbits.

*Acknowledgements.* The authors thank the anonymous referee whose report helped us to improve the original manuscript. We would furthermore like to thank Hidekazu Tanaka, Kazuhiro Kanagawa and Bertram Bitsch for inspiring discussions. AJ is grateful to the Earth-Life Science Institute (ELSI) at Tokyo Institute of Technology for hosting his research visit during March 2018. AJ further thanks the Swedish Research Council (grant 2014-5775), the Knut and Alice Wallenberg Foundation (grants 2012.0150, 2014.0017) and the European Research Council (ERC Consolidator Grant 724687-PLANETESYS) for research support. SI is supported by JSPS grant 15H02065 and MEXT grant 18H05438.

#### References

- Alexander, R. D., & Pascucci, I. 2012, *MNRAS*, 422, L82
- Armitage, P. J., Simon, J. B., & Martin, R. G. 2013, *ApJ*, 778, L14
- Ataiee, S., Baruteau, C., Alibert, Y., & Benz, W. 2018, arXiv:1804.00924
- Bai, X.-N., & Stone, J. M. 2010, *ApJ*, 722, 1437
- Bai, X.-N., & Stone, J. M. 2013, *ApJ*, 769, 76
- Bai, X.-N. 2015, *ApJ*, 798, 84
- Batalha, N. M., Rowe, J. F., Bryson, S. T., et al. 2013, *ApJS*, 204, 24
- Benítez-Llambay, P., Masset, F., Koenigsberger, G., & Szulágyi, J. 2015, *Nature*, 520, 63
- Benítez-Llambay, P., & Pessah, M. E. 2018, *ApJ*, 855, L28
- Béthune, W., Lesur, G., & Ferreira, J. 2017, *A&A*, 600, A75
- Birnstiel, T., Klahr, H., & Ercolano, B. 2012, *A&A*, 539, A148
- Bitsch, B., Morbidelli, A., Lega, E., Kretke, K., & Crida, A. 2014, *A&A*, 570, A75
- Bitsch, B., Johansen, A., Lambrechts, M., & Morbidelli, A. 2015a, *A&A*, 575, A28
- Bitsch, B., Lambrechts, M., & Johansen, A. 2015b, *A&A*, 582, A112
- Bitsch, B., & Johansen, A. 2016, *A&A*, 590, A101
- Bitsch, B., & Johansen, A. 2017, *Astrophysics and Space Science Library*, 445, 339
- Bitsch, B., Lambrechts, M., & Johansen, A. 2018a, *A&A*, 609, C2
- Bitsch, B., Morbidelli, A., Johansen, A., et al. 2018b, *A&A*, 612, A30
- Brasser, R., Bitsch, B., & Matsumura, S. 2017, *AJ*, 153, 222
- Brauer, F., Dullemond, C. P., Johansen, A., et al. 2007, *A&A*, 469, 1169
- Brauer, F., Dullemond, C. P., & Henning, T. 2008, *A&A*, 480, 859
- Brügger, N., Alibert, Y., Ataiee, S., & Benz, W. 2018, *A&A*, submitted
- Chambers, J. 2018, *ApJ*, 865, 30
- Chiang, E., & Youdin, A. N. 2010, *Annual Review of Earth and Planetary Sciences*, 38, 493
- D’Angelo, G., & Lubow, S. H. 2010, *ApJ*, 724, 730
- D’Angelo, G., & Bodenheimer, P. 2013, *ApJ*, 778, 77
- Drążkowska, J., Alibert, Y., & Moore, B. 2016, *A&A*, 594, A105
- Drążkowska, J., & Alibert, Y. 2017, *A&A*, 608, A92
- Duffell, P. C., & MacFadyen, A. I. 2013, *ApJ*, 769, 41
- Dürmann, C., & Kley, W. 2015, *A&A*, 574, A52
- Ercolano, B., & Rosotti, G. 2015, *MNRAS*, 450, 3008
- Fung, J., Shi, J.-M., & Chiang, E. 2014, *ApJ*, 782, 88
- Fung, J., & Chiang, E. 2016, *ApJ*, 832, 105
- Fung, J., & Lee, E. J. 2018, *ApJ*, 859, 126
- Goldreich, P., & Tremaine, S. 1980, *ApJ*, 241, 425
- Gomes, R., Levison, H. F., Tsiganis, K., & Morbidelli, A. 2005, *Nature*, 435, 466
- Gonzalez, J.-F., Laibe, G., & Maddison, S. T. 2017, *MNRAS*, 467, 1984
- Hallam, P. D., & Paardekooper, S.-J. 2017, *MNRAS*, 469, 3813
- Hartmann, L., Calvet, N., Gullbring, E., & D’Alessio, P. 1998, *ApJ*, 495, 385

Hasegawa, Y., Okuzumi, S., Flock, M., & Turner, N. J. 2017, *ApJ*, 845, 31  
 Hayashi, C. 1981, *Progress of Theoretical Physics Supplement*, 70, 35  
 Huang, J., Andrews, S. M., Cleeves, L. I., et al. 2018, *ApJ*, 852, 122  
 Ida, S., & Lin, D. N. C. 2004, *ApJ*, 604, 388  
 Ida, S., Guillot, T., & Morbidelli, A. 2016, *A&A*, 591, A72  
 Ida, S., & Guillot, T. 2016, *A&A*, 596, L3  
 Ida, S., Tanaka, H., Johansen, A., Kanagawa, K., & Tanigawa, T. 2018, *ApJ*, submitted  
 Ikoma, M., Nakazawa, K., & Emori, H. 2000, *ApJ*, 537, 1013  
 Izidoro, A., Morbidelli, A., Raymond, S. N., Hersant, F., & Pierens, A. 2015, *A&A*, 582, A99  
 Izidoro, A., Ogihara, M., Raymond, S. N., et al. 2017, *MNRAS*, 470, 1750  
 Johansen, A., & Klahr, H. 2005, *ApJ*, 634, 1353  
 Johansen, A., Youdin, A., & Klahr, H. 2009a, *ApJ*, 697, 1269  
 Johansen, A., Youdin, A. N., & Mac Low, M.-M. 2009b, *ApJ*, 704, L75  
 Johansen, A., Blum, J., Tanaka, H., et al. 2014, *Protostars and Planets VI*, 547  
 Johansen, A., Mac Low, M.-M., Lacerda, P., & Bizzarro, M. 2015, *Science Advances*, 1, 1500109  
 Johansen, A., & Lambrechts, M. 2017, *Annual Review of Earth and Planetary Sciences*, 45, 359  
 Kanagawa, K. D., Tanaka, H., Muto, T., Tanigawa, T., & Takeuchi, T. 2015, *MNRAS*, 448, 994  
 Kanagawa, K. D., Tanaka, H., & Szuszkiewicz, E. 2018, *arXiv:1805.11101*  
 Klahr, H., & Kley, W. 2006, *A&A*, 445, 747  
 Lambrechts, M., & Johansen, A. 2012, *A&A*, 544, A32  
 Lambrechts, M., & Johansen, A. 2014, *A&A*, 572, A107  
 Lambrechts, M., Johansen, A., & Morbidelli, A. 2014, *A&A*, 572, A35  
 Lambrechts, M., & Lega, E. 2017, *A&A*, 606, A146  
 Lambrechts, M., Lega, E., Morbidelli, A., & Nelson, R. 2018, in preparation  
 Lee, E. J., & Chiang, E. 2015, *ApJ*, 811, 41  
 Lee, E. J., & Chiang, E. 2016, *ApJ*, 817, 90  
 Lee, E. J., & Chiang, E. 2017, *ApJ*, 842, 40  
 Li, H., Lubow, S. H., Li, S., & Lin, D. N. C. 2009, *ApJ*, 690, L52  
 Lin, D. N. C., & Papaloizou, J. 1979, *MNRAS*, 186, 799  
 Lin, J. W., Lee, E. J., & Chiang, E. 2018, *MNRAS*, 480, 4338  
 Liu, B., Ormel, C. W., & Lin, D. N. C. 2017, *A&A*, 601, A15  
 Liu, B., & Ormel, C. W. 2018, *arXiv:1803.06149*  
 Lodders, K. 2004, *ApJ*, 611, 587  
 Lubow, S. H., & D'Angelo, G. 2006, *ApJ*, 641, 526  
 Lyra, W., Johansen, A., Klahr, H., & Piskunov, N. 2008, *A&A*, 479, 883  
 Lyra, W., Johansen, A., Klahr, H., & Piskunov, N. 2009, *A&A*, 493, 1125  
 Lyra, W., Paardekooper, S.-J., & Mac Low, M.-M. 2010, *ApJ*, 715, L68  
 Madhusudhan, N., Bitsch, B., Johansen, A., & Eriksson, L. 2017, *MNRAS*, 469, 4102  
 Matsumura, S., Brasser, R., & Ida, S. 2017, *A&A*, 607, A67  
 Menu, J., van Boekel, R., Henning, T., et al. 2014, *A&A*, 564, A93  
 Morbidelli, A., Lambrechts, M., Jacobson, S., & Bitsch, B. 2015, *Icarus*, 258, 418  
 Mordasini, C. 2014, *A&A*, 572, A118  
 Mulders, G. D., & Dominik, C. 2012, *A&A*, 539, A9  
 Muñoz Caro, G. M., & Schutte, W. A. 2003, *A&A*, 412, 121  
 Musiolik, G., Teiser, J., Jankowski, T., & Wurm, G. 2016a, *ApJ*, 818, 16  
 Musiolik, G., Teiser, J., Jankowski, T., & Wurm, G. 2016b, *ApJ*, 827, 63  
 Ndugu, N., Bitsch, B., & Jurua, E. 2018, *MNRAS*, 474, 886  
 Okuzumi, S., Tanaka, H., Kobayashi, H., & Wada, K. 2012, *ApJ*, 752, 106  
 Ormel, C. W., & Cuzzi, J. N. 2007, *A&A*, 466, 413  
 Ormel, C. W., & Klahr, H. H. 2010, *A&A*, 520, A43  
 Ormel, C. W., Liu, B., & Schoonenberg, D. 2017, *A&A*, 604, A1  
 Owen, J. E., & Wu, Y. 2017, *ApJ*, 847, 29  
 Paardekooper, S.-J., Baruteau, C., Crida, A., & Kley, W. 2010, *MNRAS*, 401, 1950  
 Pérez, L. M., Carpenter, J. M., Chandler, C. J., et al. 2012, *ApJ*, 760, L17  
 Pinte, C., Dent, W. R. F., Ménard, F., et al. 2016, *ApJ*, 816, 25  
 Piso, A.-M. A., & Youdin, A. N. 2014, *ApJ*, 786, 21  
 Popovas, A., Nordlund, Å., Ramsey, J. P., & Ormel, C. W. 2018, *MNRAS*, 479, 5136  
 Pringle, J. E. 1981, *ARA&A*, 19, 137  
 Qi, C., Öberg, K. I., Wilner, D. J., et al. 2013, *Science*, 341, 630  
 Rafikov, R. R. 2002, *ApJ*, 572, 566  
 Ros, K., & Johansen, A. 2013, *A&A*, 552, A137  
 Safronov, V. S. 1969, *Evolutsiia doplanetnogo oblaka*. (English transl.: Evolution of the Protoplanetary Cloud and Formation of Earth and the Planets, NASA Tech. Transl. F-677, Jerusalem: Israel Sci. Transl. 1972)  
 Schoonenberg, D., & Ormel, C. W. 2017, *A&A*, 602, A21  
 Shiraishi, M., & Ida, S. 2008, *ApJ*, 684, 1416  
 Tanaka, H., & Ida, S. 1999, *Icarus*, 139, 350  
 Tanaka, H., Takeuchi, T., & Ward, W. R. 2002, *ApJ*, 565, 1257  
 Tanigawa, T., & Tanaka, H. 2016, *ApJ*, 823, 48

Wahl, S. M., Hubbard, W. B., Militzer, B., et al. 2017, *Geophys. Res. Lett.*, 44, 4649  
 Weidenschilling, S. J. 1977, *MNRAS*, 180, 57  
 Youdin, A., & Goodman, J. 2005, *ApJ*, 620, 459  
 Zsom, A., Ormel, C. W., Güttler, C., Blum, J., & Dullemond, C. P. 2010, *A&A*, 513, A57

## Appendix A: Analytical expression for the growth track time

In this Appendix we derive the time associated with the analytical growth track derived in Section 2. We replace the pebble surface density  $\Sigma_p$  in equation (1) by equation (13) and split out the specific dependence on  $M$  and  $r$  to obtain

$$\dot{M} = 2 \left( \frac{\text{St}}{0.1} \right)^{2/3} GM_\star (3M_\star)^{-2/3} \times \frac{\xi \dot{M}_g(t)}{2\pi[\chi \text{St} + (3/2)\alpha]c_{s1}^2 \text{AU}^\zeta} M^{2/3} r^{\zeta-1}. \quad (\text{A.1})$$

We need now a model for the evolution of the protoplanetary disc. We use the standard  $\alpha$ -disc evolution model of Section 3. The turbulent viscosity follows the power-law

$$\nu = \alpha c_s H \propto r^\gamma. \quad (\text{A.2})$$

Here the power-law index  $\gamma$  can be written as

$$\gamma = (3/2) - \zeta. \quad (\text{A.3})$$

The gas accretion onto the star evolves as (Hartmann et al., 1998)

$$\dot{M}_g = \dot{M}_{g0} T^{-(5/2-\gamma)/(2-\gamma)}, \quad (\text{A.4})$$

where the non-dimensional time is

$$T = t/t_s + 1, \quad (\text{A.5})$$

the characteristic time is

$$t_s = \frac{1}{3(2-\gamma)^2} \frac{R_1^2}{\nu_1}, \quad (\text{A.6})$$

and  $R_1$  is the initial disc size and  $\nu_1$  the viscosity at that location. We now insert the inverse solution for the growth track,  $r(M)$ , and separate the variables  $M$  and  $r$  to yield the equation

$$r_0^{1-\zeta} M^{-2/3} \left( 1 - \frac{M^{4/3} - M_0^{4/3}}{M_{\text{max}}^{4/3} - M_0^{4/3}} \right) dM = \frac{2(\text{St}/0.1)^{2/3} GM_\star (3M_\star)^{-2/3} \xi \dot{M}_{g0}}{2\pi[\chi \text{St} + (3/2)\alpha]c_{s1}^2 \text{AU}^\zeta} T^{-(5/2-\gamma)/(2-\gamma)} t_s dT. \quad (\text{A.7})$$

We integrate both sides to yield

$$r_0^{1-\zeta} \left[ \frac{-(3/5)(M^{5/3} - M_0^{5/3}) + 3(M^{1/3} - M_0^{1/3})M_{\text{max}}^{4/3}}{M_{\text{max}}^{4/3} - M_0^{4/3}} \right] = \frac{2(\text{St}/0.1)^{2/3} GM_\star (3M_\star)^{-2/3} \xi \dot{M}_{g0}}{2\pi[\chi \text{St} + (3/2)\alpha]c_{s1}^2 \text{AU}^\zeta} \times \frac{[T^{-(5/2-\gamma)/(2-\gamma)+1} - T_0^{-(5/2-\gamma)/(2-\gamma)+1}] t_s}{-(5/2-\gamma)/(2-\gamma)+1}. \quad (\text{A.8})$$

We now divide the equation by the solution at  $r = 0$ ,  $M(T_{\max}) = M_{\max}$ , to give the simpler expression

$$\frac{-(3/5)(M^{5/3} - M_0^{5/3}) + 3(M^{1/3} - M_0^{1/3})M_{\max}^{4/3}}{-(3/5)(M_{\max}^{5/3} - M_0^{5/3}) + 3(M_{\max}^{1/3} - M_0^{1/3})M_{\max}^{4/3}} = \frac{T^{-(5/2-\gamma)/(2-\gamma)+1} - T_0^{-(5/2-\gamma)/(2-\gamma)+1}}{T_{\max}^{-(5/2-\gamma)/(2-\gamma)+1} - T_0^{-(5/2-\gamma)/(2-\gamma)+1}}. \quad (\text{A.9})$$

Note that  $T_{\max}$  may be complex if the planet never reaches  $r = 0$ . The solution can easily be solved for  $T$  for a given  $M$ , which can be converted to  $t$  using the viscous disc expression from equation (A.5). The analytical expression for  $T_{\max}$  is obtained by inserting  $M = M_{\max}$  in equation (A.8).

If we assume for simplicity that  $\dot{M}_g$  is constant, then we can replace the complicated function of  $T$  appearing on the right-hand-side of equation (A.8) by  $t - t_0$ . In that case (setting  $M_0 = t_0 = 0$  also) we have for  $t_{\max}$  the simple expression

$$t_{\max} = r_0^{1-\zeta} (12/5) M_{\max}^{1/3} \times \frac{2\pi(3/2)[(2/3)(\text{St}/\alpha)\chi + 1]\alpha c_{s1}^2 \text{AU}^\zeta}{2(\text{St}/0.1)^{2/3} G M_\star (3M_\star)^{-2/3} \xi \dot{M}_{g0}}. \quad (\text{A.10})$$

The time-evolution of the growth track follows in the limit  $M_0 = t_0 = 0$  as  $t/t_{\max} = (5/3)(M/M_{\max})^{1/3} - (1/4)(M/M_{\max})^{5/3}$ . We can scale the time-scale to migrate to the star,  $t_{\max}$ , to typical disc values,

$$t_{\max} = 0.29 \text{ Myr} \left\{ \frac{[(2/3)(\text{St}/\alpha)\chi + 1]/2.9}{(\text{St}/0.01)^{2/3}} \right\} \left( \frac{\xi}{0.01} \right)^{-1} \times \left( \frac{M_\star}{M_\odot} \right)^{-1/3} \left( \frac{c_{s1}}{6.5 \times 10^2 \text{ m s}^{-1}} \right)^2 \times \left( \frac{\alpha}{0.01} \right) \left( \frac{\dot{M}_{g0}}{10^{-7} M_\odot \text{ yr}^{-1}} \right)^{-1} \times \left( \frac{M_{\max}}{10 M_E} \right)^{1/3} \left( \frac{r_0}{25 \text{ AU}} \right)^{1-\zeta}. \quad (\text{A.11})$$

The relevant value of  $M_{\max}$  for the given parameters can be inserted from equation (23). However, we note that  $t_{\max}$  depends weakly on the maximum mass, as  $M_{\max}^{1/3}$ . Hence the parameter dependencies in equation (23) are much weaker than those explicit in equation (A.11) above. One can also approximately use  $t_{\max}$  as the time to reach the isolation mass, as the isolation mass and the maximum mass are both reached after significant migration when  $r_0 \gg 10 \text{ AU}$ . Under all circumstances does  $t_{\max}$  give an upper limit to the time of reaching the isolation mass.